MATERIALS SCIENCE

Rapid liquid phase–assisted ultrahigh-temperature sintering of high-entropy ceramic composites

Hua Xie[1,2]†, Mingde Qin[3]†, Min Hong[1,2]†, Jiancun Rao[4], Miao Guo[1,2], Jian Luo[3]*, Liangbing Hu[1,2]*

High-entropy ceramics and their composites display high mechanical strength and attractive high-temperature stabilities. However, properties like strong covalent bond character and low self-diffusion coefficients make them difficult to get sintered, limiting their mass popularity. Here, we present a rapid liquid phase–assisted ultrahigh-temperature sintering strategy and use high-entropy metal diboride/boron carbide composite as a proof of concept. We use a carbon-based heater to fast-heat the composite to around 3000 K, and a small fraction of eutectic liquid was formed at the interface between high-entropy metal diborides and boron carbide. A crystalline dodecaboride intergranular phase was generated upon cooling to ameliorate the adhesion between the components. The as-sintered composite presents a high hardness of 36.4 GPa at a load of 0.49 N and 24.4 GPa at a load of 9.8 N. This liquid phase–assisted rapid ultrahigh-temperature strategy can be widely applicable for other ultrahigh-temperature ceramics as well.

INTRODUCTION

High-entropy ceramics—such as high-entropy borides (HEBs; containing five or more different metal borides) (*1*–*3*), oxides (*4*), carbides (*5*, *6*), nitrides (*4*, *7*), and their composites—have recently received attention because of their attractive properties, including high melting points, high mechanical moduli, and good oxidation resistance (*8*, *9*), which make them promising candidates for applications in high-temperature environments (*10*–*12*). As a new category of ultrahigh-temperature ceramics, HEBs can be synthesized in different ways including by reactive sintering of multiple commercial binary borides (*1*), through the reduction of metal oxides with boron (*13*), and via boron-metal reactive sintering (*2*). Compared to conventional binary boride ceramics, HEBs feature improved hardness and oxidation resistance (*1*). Increasing the density of high-entropy ceramics can also elevate their mechanical properties, such as hardness (*14*). However, it is difficult to rapidly densify these ceramics because of the high covalent bond content and extremely low elemental diffusion coefficients (e.g., 10^{-20} m^2/s, even at 2200 K) (*15*–*18*). As a result, long exposure times to a temperature range of 2000 to 2200 K along with the introduction of sintering additives are required to achieve densified borides by conventional ambient-pressure sintering approaches (*16*, *17*). For example, the use of sintering additives such as boron carbide can react and remove the oxide impurities in the borides, which impede densification by forming more volatile species (*19*–*23*). However, mechanical properties of the composites, such as the hardness, show no pronounced improvement even as the mass ratio of boron carbide or other additives is substantially increased under conventional sintering scenarios, which might be owing to the entrapped porosity present in additives (*24*, *25*). Other factors such as the inconsistency of the thermal expansion coefficients of the matrix and additive components can further exacerbate the interface mismatches between the diboride and additive phases (*26*–*28*), compromising the mechanical properties of the composites.

Various strategies have been investigated to improve the densification of the composites. For example, approaches that elevate the treatment temperature to above the melting point, such as arc melting (*29*–*31*), or by exerting an external pressure, such as hot pressing (*32*–*34*), can ameliorate the casting or sintering results of these ultrahigh-temperature ceramic composites. However, these methods can be difficult to apply for objects with ultrathin or complex geometries because they can destroy the geometry by either melting it or crushing it. Furthermore, techniques that rely on completely melting the HEB have difficulty retaining the material's uniformity for high-entropy compositions because of the inevitable microsegregation of different compositions that occurs during solidification. The temperature for conventional furnace sintering or commonly used hot pressing would frequently not exceed 2500 K (*3*, *33*), and the temperature for melting methods would often be higher than 3300 K to ensure the complete melting of the high-temperature ceramics. There is a huge temperature gap in between these approaches, and we can develop sintering methods in this high-temperature range to overcome the low diffusion coefficients and improve the densification, as well as elevate the overall mechanical performance of the HEB.

Here, we present a rapid liquid-phase sintering strategy that improves the densification of high-entropy, high-temperature ceramics without losing their high-entropy structure. We heat the ceramics at temperatures greater than what can be achieved using a conventional furnace or hot pressing (~2500 K), but lower than the ultrahigh temperatures achieved by techniques such as arc melting (~3300 K), which helps to promote effective densification but without completely melting the material, thus preserving the high-entropy structure.

RESULTS

For a proof of concept, we mixed a composite of an HEB metal diboride [$(Ti_{0.2}Ta_{0.2}Mo_{0.2}W_{0.2}Zr_{0.2})B_2$] with a boron carbide additive and used carbon-based Joule heaters to rapidly heat the composite to an ultrahigh yet controlled temperature of ~3000 K for

[1]Department of Materials Science and Engineering, University of Maryland, College Park, MD 20742, USA. [2]Center for Materials Innovations, University of Maryland, College Park, MD 20742, USA. [3]Department of NanoEngineering, University of California San Diego, La Jolla, CA 92093, USA. [4]Advanced Imaging and Microscopy Laboratory of Maryland NanoCenter, University of Maryland, College Park, MD 20742, USA.
*Corresponding author. Email: binghu@umd.edu (L.H.); jluo@alum.mit.edu (J.L.)
†These authors contributed equally to this work.

approximately 2 min in the ambient gas pressure environment (Fig. 1A). At this temperature, while the primary solid HEB phase is maintained, at the interface, HEB and boron carbide form a eutectic liquid that can penetrate and fill the voids between the grains and lead to the formation of a low–melting point intergranular Zr-rich dodecaboride (ZrB_{12}) phase. High-resolution transmission electron microscopy (HRTEM) revealed that the boron carbide phase can form coherent structures with the HEB, suggesting that the HEB grain surface provides nucleation sites and guides the grain growth for the boron carbide during the cooling process. The composite ceramic presents a high hardness and can reach 36.4 GPa at an initial load of 0.49 N while still maintaining a value of 24.4 GPa when the load is increased to 9.8 N. We carefully control the local temperature under the melting points of the HEB to avoid damaging the geometry of the composite sample, whereas the temperature is set notably higher than that with conventional sintering methods to promote the formation of the eutectic liquid. Our sintering strategy has filled the temperature gap between conventional furnace methods

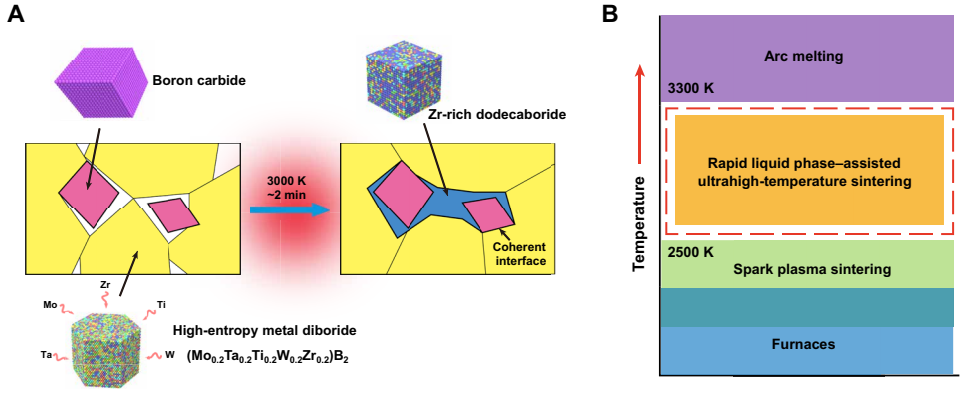

Fig. 1. Sintering schematic and comparison with conventional approaches. (**A**) Schematic demonstrating the rapid liquid phase–assisted ultrahigh-temperature sintering process. The HEB/boron carbide composite is heated up to 3000 K for ~2 min in an atmospheric pressure environment, which results in the formation of a low–melting point ZrB_{12}-based intergranular phase that bonds with the HEB and boron carbide after cooling. (**B**) This sintering strategy has filled the temperature gap in conventional sintering approaches.

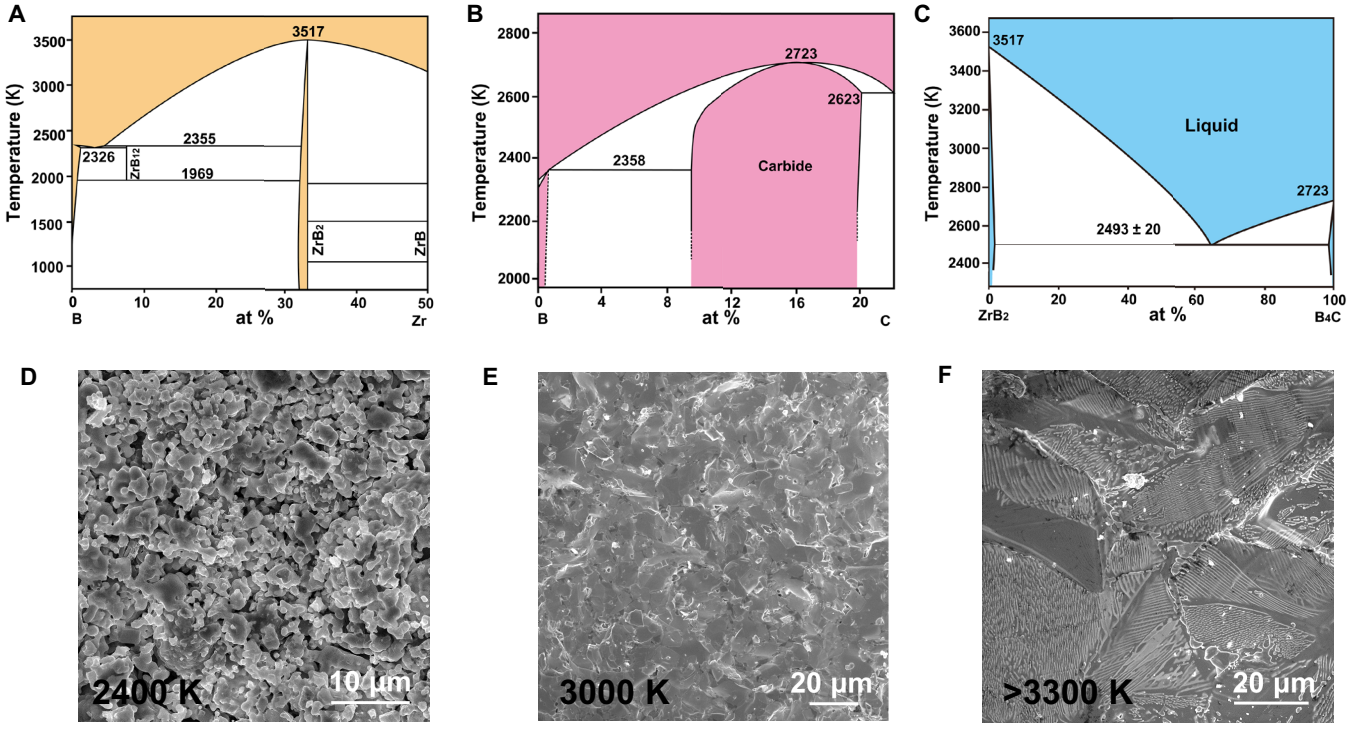

Fig. 2. The influence of temperature and phases on the sintering results. Phase diagrams of the (**A**) B-Zr, (**B**) B-C, and (**C**) ZrB_2-B_4C components (*36*, *38*, *41*). At 3000 K, the high-entropy metal diborides can maintain a solid state, while the boron carbide couples with the HEB to form the eutectic liquid phase. Scanning electron microscopy (SEM) images showing the morphologies of the composite samples at different sintering temperatures of (**D**) 2400 K, (**E**) 3000 K, and (**F**) above 3300 K. The optimal temperature here for the rapid sintering of the HEB composite is around 3000 K. at %, atomic %.

and arc melting (Fig. 1B), offering a more flexible approach for the sintering of high-temperature ceramics, particularly for objects with ultrathin or complex geometries.

The synthesis process begins by mixing elemental boron and transition metal powders (Mo, Zr, Ta, Ti, and W) and heating the materials to 2000 K in an argon-filled environment to trigger the self-propagating exothermic reactions for the synthesis of the HEB. Excessive boron powder and Ketjenblack carbon were added to ensure the complete removal of volatilizable oxide impurities (e.g., B_2O_3) and the in situ synthesis of boron carbide. The HEB/boron carbide composite powders acquired above (fig. S1) were further pressed into pellets, and the rapid liquid-phase high-temperature sintering process was conducted as the treatment temperature was elevated to 3000 K by a carbon-based heater and maintained for 2 min (see details in Materials and Methods). Phase diagrams of Zr-B (Fig. 2A), Ta-B, and Ti-B (fig. S2, A and B) (*35*–*41*) demonstrate that at 3000 K, the main HEB phase can maintain its solid state, while boron carbide (Fig. 2B) melts when the temperature is higher than 2723 K and forms a eutectic liquid with the HEB. Other elements from the HEB, such as W and Mo (fig. S2, C and D), that cannot form AlB_2-type diborides can dissolve in and become stabilized in the HEB as a substitutional solid solution at higher temperatures, which is confirmed by our previous results (*2*). The eutectic liquid features a lower solidification point than the HEB (Fig. 2C and fig. S3), and a new intergranular-phase ZrB_{12} can form, filling in the voids between HEB and boron carbide grains after cooling down (~2355 K; Fig. 2A).

To evaluate the impact of the sintering temperature on the composite morphology, we sintered the composite at different temperatures. Figure 2 (D to F) presents the resulting fractured cross-sectional surface scanning electron microscopy (SEM) images of the composite samples sintered at 2400, 3000, and 3300 K, respectively. When the sintering temperature was set to ~2400 K (Fig. 2D), similar to that of conventional furnaces, the sintering driving force of the reduction in surface energy is rather low, as the SEM image shows that the composite powder still maintains the porous geometry, although we observed some necking effect. The results suggest that not enough eutectic liquid is formed at the temperature of ~2400 K and that longer heat treatment duration is needed to densify the composite.

However, when the sintering temperature is elevated to 3000 K (Fig. 2E), HEB can maintain its solid state, and the eutectic liquid is well confined in between the HEB grains. As indicated in the SEM image, the ceramic composite is well sintered in a short time. When we continue increasing the temperature to 3300 K, the eutectic liquid amount is substantial, and HEB framework starts to melt, which is further exacerbated by the plasma generated by the carbon heater at this temperature range in the argon environment. As a result, the

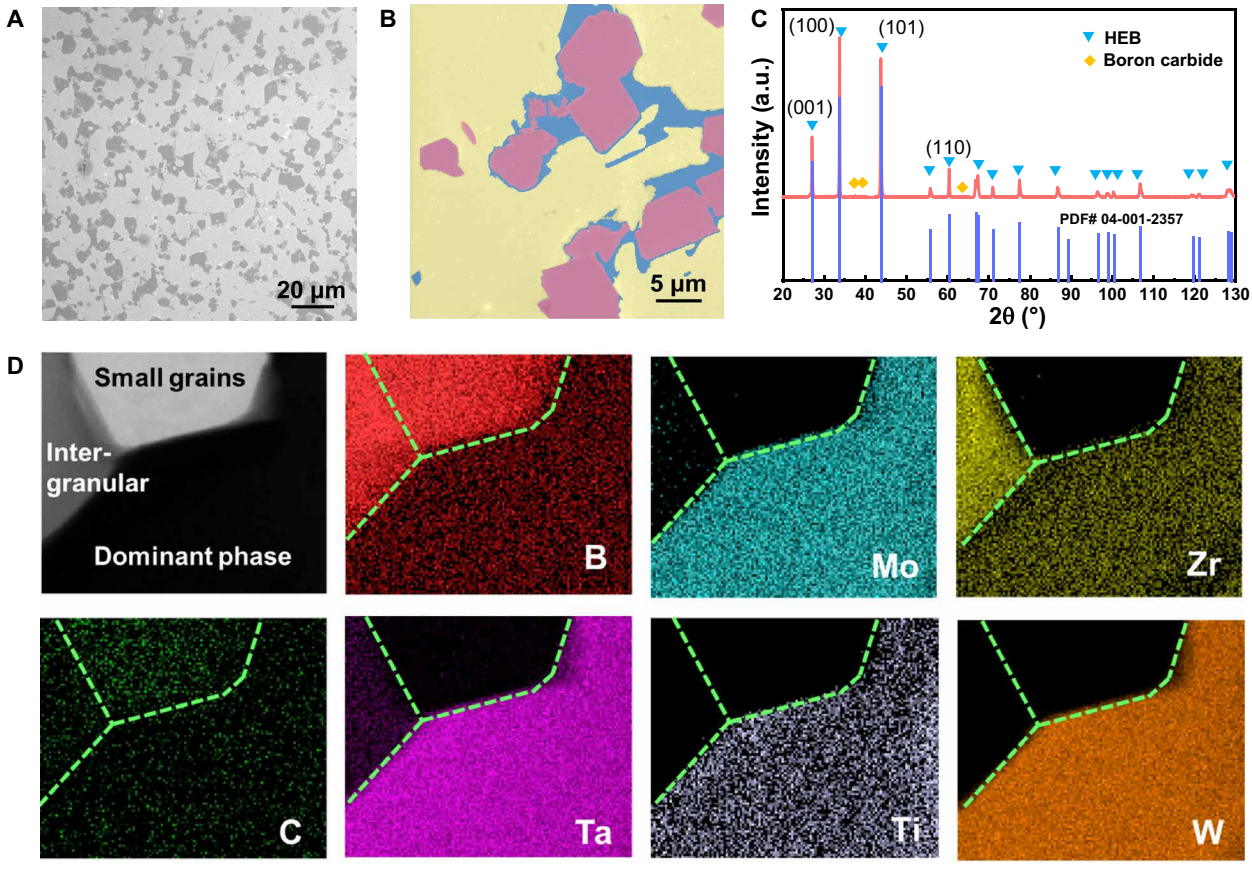

Fig. 3. Composition analysis. (**A**) The polished cross-sectional SEM image of the synthesized composite. (**B**) SEM image with false colors to delineate the three different phases. (**C**) XRD patterns of the synthesized composite. HEB dominates the peak signals due to the high *Z* values and electron density of the transition metal elements. (**D**) TEM image of the grains and EDS mapping of the different elements, including B, Mo, Zr, C, Ta, Ti, and W, respectively. The dominant phase is the HEB with Mo, Zr, Ta, Ti, and W uniformly distributed, and the small grains belong to boron carbide. a.u., arbitrary units.

sample is unable to maintain its original geometry and becomes a spherical ingot after the temperature is gradually cooled down, which resembles the samples achieved via arc melting method (fig. S4). Dendrite arms observed in the SEM image (Fig. 2F) indicate a noticeable solute redistribution. Such microsegregation of the elements can decrease the element distribution uniformity in the HEB. Therefore, the optimal temperature here for the rapid sintering of the HEB composite is around 3000 K as it balances the need to form the eutectic liquid for the liquid phase–assisted sintering without simultaneously melting the composite.

To achieve the rapid sintering result, we carefully tailored the temperature to ~3000 K in view of the component phase diagrams to accelerate the densification process without melting the whole sample. The final sintered pellets at 3000 K were then cut and polished for further detailed characterization. SEM revealed the polished cross-sectional surface of the sintered composite, which featured an apparent density of around 99% calculated on the SEM results (Fig. 3A and fig. S5). The three phases present different contrasts due to the electron signals carrying backscattered electron information captured by the Everhart-Thornley detector. Figure 3B shows a zoomed-in SEM image with false colors to delineate the three different phases: the dominant phase (shown in yellow), secondary phase (magenta), and an intergranular phase (blue). The intergranular phase (volume ratio, 8.9%) occurs at the boundary regions between the dominant phase (volume ratio, 66.5%) and the smaller-grain secondary phase (volume ratio, 23.6%) after the rapid high-temperature sintering. Figure 3C presents x-ray powder diffraction (XRD) patterns of the synthesized ceramic composite. The dominant phase belongs to the HEB (*42*), but because of the relatively small atomic numbers (*Z*) and low electron density of the boron and carbon elements, the diffraction peaks of other compositions are overwhelmed by the much stronger peaks from the HEB phase.

To further evaluate and analyze the compositional distribution of the different grains, we used the focus ion beam (FIB) technique to slice a thin composite layer of ~60 nm in thickness for TEM analysis (fig. S6). Figure 3D and fig. S7 show the energy-dispersive x-ray spectroscopy (EDS) mapping of the three different phases. The mapping results confirm the boron carbide grains (with the boron element dominating the composition), whereas Zr and B elements make up the intergranular phase with remnant elements such as Ta and Mo, which should be a ZrB_{12} based phase according to the phase diagram analysis above (Fig. 2A). In the HEB phase, all the transition metal elements are uniformly distributed to corroborate the high-entropy state, which appears darker in the TEM image because of

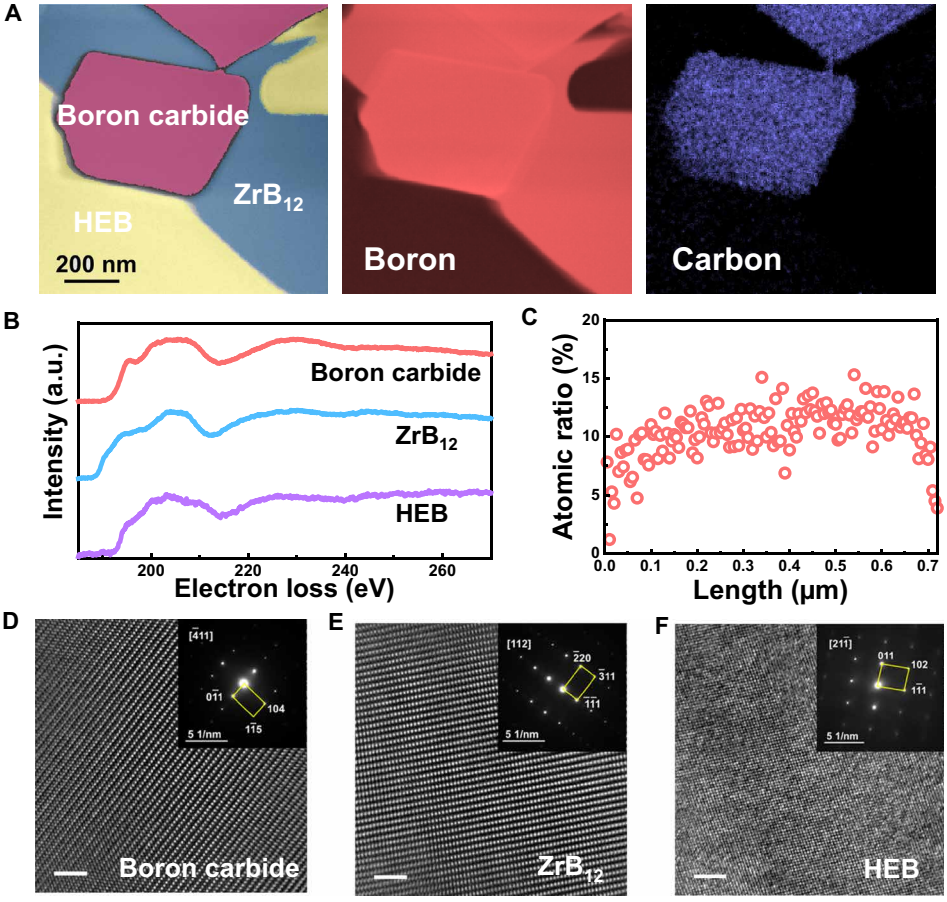

Fig. 4. EELS and electron diffraction analysis of the phases. (**A**) STEM image with false colors (boron carbide, magenta; ZrB_{12}, blue; and HEB, yellow) and EELS mapping of the boron and carbon element distribution. (**B**) EELS B-K edges for the three different grains. (**C**) Carbon atomic ratio across a boron carbide grain, which indicates a composition of $B_{13}C_2$ here. (**D** to **F**) HRTEM of the grains from boron carbide, ZrB_{12}, and HEB, together with their corresponding SAED patterns, which further confirmed their crystal lattice structures: $B_{13}C_2$ (space group: *R*-3*m*, PDF number: 03-065-6874) (*47*), ZrB_{12} (space group: *Fm*-3*m*, PDF number: 04-003-5571) (*48*), and HEB (space group: *P*6/*mmm*, PDF number: 04-001-2357 AlB_2 type) (*42*). Scale bars, 2 nm.

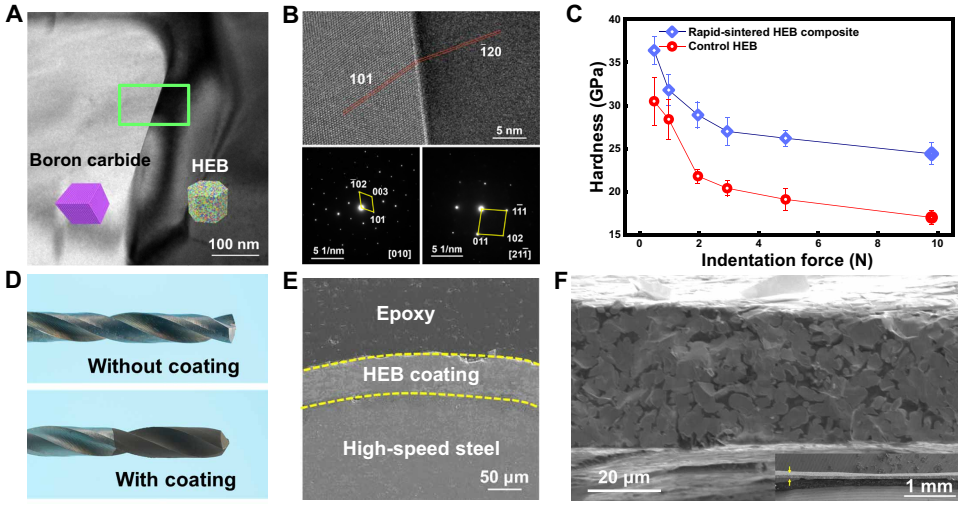

Fig. 5. Mechanical properties and sintering demonstrations. (**A**) TEM image showing the interface between the boron carbide and HEB grains. (**B**) One coherent interface between two grains of boron carbide and HEB. The zone axis [010] of the boron carbide is parallel to the [21$\bar{1}$] zone axis of the HEB, while the (101) plane of the boron carbide is coherent with the ($\bar{1}$20) plane of the HEB. The coherent interface can further improve the adhesion between the two components. (**C**) The Vickers hardness of the eutectic liquid–assisted ultrahigh-temperature sintered composite is substantially improved in comparison with that of the HEB without boron carbide and intergranular ZrB_{12} phases. (**D**) Photos of a drill bit with and without HEB composite coating. (**E**) Cross-sectional SEM image showing the HEB composite coating on the drill bit. (**F**) The free-standing HEB composite membrane with a thickness of 50 μm. The inset is a SEM image showing the membrane with smaller magnification.

their stronger electron scattering capabilities. Although the boron carbide phase was directly formed via the reaction between the elemental boron and the carbon black during the self-propagation reaction, EDS mapping could not completely resolve the carbon distribution because of its relatively weak signal.

DISCUSSION

Because of the similarity in both electronic and nuclear scattering cross sections for boron and carbon atoms, it is difficult to resolve their exact occupation in the grains with the TEM-EDS analysis above. In addition, boron carbide usually has variable stoichiometric ratios (*36*), and the specific composition ratio of boron and carbon should be determined for the specific grains. To further investigate the distribution of light element boron and carbon in the FIB-prepared sample, electron energy-loss spectroscopy (EELS) was conducted to evaluate the borides and boron carbide grains. Figure 4A presents a scanning transmission electron micrograph (STEM) of the three phases with false colors (magenta, blue, and yellow representing the boron carbide, ZrB_{12}, and HEB phases, respectively), as well as the EELS mapping to show the compositional distribution of the B and C elements. The boron carbide and ZrB_{12} phases present prominent B-rich structures (*43*, *44*), consistent with the EDS results above, whereas the carbon element signal is essentially confined to the boron carbide grains, which indicates that no other transition metal carbides were formed. The EELS B-K fine structure profiles from the three phases (Fig. 4B) with different chemical shifts of the edges for the grains indicate the different valent states of the boron atoms (*10*, *45*, *46*). The dodecaboride ZrB_{12}-based phase contains a B_{12} cube-octahedra structure, resulting in a very different energy-loss onset profile from that of the boron carbide and HEB (*10*). We measured the carbon atomic ratio across a boron carbide grain (Fig. 4C) and found that the value fluctuated from 10 to 15% and dropped precipitously at the grain boundaries. X-ray photoelectron spectroscopy (fig. S8) further corroborated the existence of multichemical states of the boron element in the HEB, ZrB_{12}, and boron carbide.

Figure 4 (D to F) shows HRTEM images of the three different phases and their corresponding selected-area electron diffractions (SAEDs). The fast Fourier transform of the boron carbide lattice and its SAED (Fig. 4D) further confirmed that it displays a structure of $B_{13}C_2$ [space group: *R*-3*m*, powder diffraction file (PDF) number: 03-065-6874] (*47*), as also validated by the EELS analysis above. The HRTEM and SAED patterns also further confirm the ZrB_{12}'s rhombohedral structure (space group: *Fm*-3*m*, PDF number: 04-003-5571; Fig. 4E) (*48*), consistent with the EDS and phase diagram analysis above. Meanwhile, the HEB phase features a hexagonal structure with a space group of *P*6/*mmm* (PDF number: 04-001-2357 AlB_2 type; Fig. 4F) (*42*), in which the transition metal ions are intercalated between sheets of the layered boron atom structure. More SAED results are listed in the Supplementary Materials for the phase analysis during the calculation of phase structures (figs. S9 to S11). The electron backscatter diffraction (EBSD) technique was used to measure the grain sizes and crystal orientations of the HEB and ZrB_{12} phases. Figure S12A presents the EBSD normal-direction inverse–pole figure orientation maps, and the grain size distributions of the HEB and ZrB_{12} phases are shown in fig. S12 (B and C, respectively).

The rapid ultrahigh-temperature sintering technique not only can create the eutectic liquid phase for the fast densification but also helps improve the interfaces between the boron carbide and HEB. Coherent interface can be found in the composite, as shown in Fig. 5A. The HRTEM image (Fig. 5B) and SAEDs indicate that the boron carbide and HEB grains can have coherent interfaces, as the zone axis [010] of $B_{13}C_2$ is parallel to the [21$\bar{1}$] zone axis of HEB and the (101) plane of boron carbide is coherent with the ($\bar{1}$20) plane of HEB. This coherent structure indicates that the HEB surface provides nucleation sites that guide the grain growth of the boron carbide, which can further improve the interfacial binding between the

two components. We further conducted Vickers hardness experiments to evaluate the effectiveness of this eutectic liquid–assisted ultrahigh-temperature sintering approach (Fig. 5C). We used the same ultrahigh-temperature sintering approach to synthesize a HEB without boron carbide and intergranular ZrB_{12} phases (detailed characterization can be found in fig. S13). The rapid high-temperature sintered composite features a hardness of 36.4 GPa at a loading force of 0.49 N and can maintain a good value of 24.4 GPa even after the load is elevated to 9.8 N, much higher than that of the HEB without boron carbide and intergranular ZrB_{12} phases. The prominent hardness improvement suggests that the rapid eutectic liquid–assisted ultrahigh-temperature sintering technique improves the densification of the composite.

Our rapid sintering approach also presents applicable in the synthesis of coatings or ultrathin free-standing membranes. Figure 5D shows the photos of a drill bit with and without the HEB composite coating, and Fig. 5E presents the cross-sectional image of the HEB composite coating achieved via multiple-pulse ultrahigh-temperature sintering. Figure 5F depicts a free-standing HEB composite membrane with a thickness of around 50 μm, which usually cannot be achieved by conventional spark plasma sintering or arc melting methods.

In summary, we have demonstrated a rapid liquid phase–assisted ultrahigh-temperature sintering technique for high-temperature ceramic composites. Taking the HEB composite as a proof of concept, the temperature was carefully controlled at 3000 K to maintain the HEB solid state while also producing a small fraction of eutectic liquid to enable liquid-phase sintering. Upon cooling, a low–melting point ZrB_{12} intergranular phase was further formed to fill the voids between the HEB and boron carbide. HRTEM revealed that the boron carbide phase presents good coherent structures with the HEB, which benefits the interfacial adhesion between the two components. The composite ceramic presents a prominently increased hardness of 36.4 GPa at an indentation load of 0.49 N and still maintains a high value of 24.4 GPa when the load is further increased to 9.8 N, which is higher than that of the HEB without boron carbide and the intergranular ZrB_{12} phase. Our rapid ultrahigh-temperature sintering approach can successfully overcome the low diffusion coefficients of the ceramics to promote effective densification and enables the sintering of coatings or free-standing high-temperature ceramic membranes, which could not be easily achieved by conventional spark plasma sintering or arc melting methods. This strategy also opens new opportunities to sinter other ultrahigh-temperature ceramic composites such as carbides, nitrides, and silicides.

MATERIALS AND METHODS

Carbon-based Joule heat sintering setup

The Joule heating components are composed of two pieces of carbon felt strips. An alumina plate was used to fix the carbon felt. Copper tape was attached on the alumina stage as the current collectors, and silver paste was used to connect the carbon felt strips and the copper current collectors to decrease the contact resistance. A VOLTEQ supply was used as the DC power source to elevate the temperature of the Joule heating components with a tunable current (0 to 50 A) and voltage (0 to 100 V). The temperature was calculated from the ultraviolet-visible spectra captured with a Vision Research Phantom Miro M110 high-speed camera. The temperature error bar is of approximately ±100°C (*49*).

Preparation of the HEB composite powder

The boron and transition metal elemental powders were weighed at a nominal ratio of $(Mo_{0.2}Ta_{0.2}Ti_{0.2}W_{0.2}Zr_{0.2})B_2$, mixed, and ball-milled for 5 hours. Additional 80 mole percent (mol %) excess boron elemental powder and 7 mol % Ketjenblack carbon were added to compensate for the evaporative loss of boron oxide during HEB formation reactions and for the in situ synthesis of boron carbide. The ball-milling jars were sealed in Ar environment to avoid the oxidation of the elementary powders. The well–ball-milled powder was transferred and uniformly piled in between the two carbon felt heaters in an Ar-filled glovebox. The heat ramp rate and temperature of the carbon heater were carefully controlled via the DC power supply (maximum power of 5000 W). The temperature was rapidly elevated to 2000 K to trigger the self-propagating reactions.

Preparation of the sintered composite pellets

The powder after the self-propagating reaction was milled and pressed into pellets with a diameter of 8 mm, which were sandwiched by the carbon felt heater. The temperature was then elevated to 2400, 3000, or 3300 K to sinter the pellet. The heating duration lasted for 2 min, and the power supply was turned off before the sample pellets were cooled down to room temperature. The sintered pellets were broken in half before further characterization.

Materials characterization

The morphology of the pellet surface was evaluated on a Tescan XEIA Plasma FIB/scanning electron microscope. XRD of the electrolyte was performed on a D8 Bruker Advanced X-ray Diffraction system using a Cu Kα radiation source operated at 40 kV and 40 mA. The scattering angles were from 20° to 130°. The Cu $K\alpha_1$ wavelength was 1.54059 Å.

TEM specimens were prepared by an in situ lift-out technique in a dual-beam system (GAIA3, Tescan, Czech Republic). First, a piece of the studied materials was mechanically ground and polished. Then, a slice with dimensions of 20 μm by 10 μm by 2 μm was cut off from the finely polished surface of the bulk material by the FIB with a Ga^+ source operated at 30 keV and 3 nA. The slice was then transferred to a TEM grid for further thinning by FIB with step-decreasing acceleration voltages and currents. Last, the lamella was polished at 5 keV and 15 pA until it was ~80 nm thick. The subsequent TEM study was carried out in a JEM 2100F equipped with Bruker EDS and Gatan EELS/GIF systems operating at 200 keV for the characterization of the interfaces between the boron carbide and HEB grains.

Hardness measurement

Vickers microhardness measurement was conducted on a diamond indenter with multiple loading forces, starting from 0.49 N and a holding time of 15 s and further increased to 9.80 N following American Society for Testing and Materials (ASTM) C1327 (*50*). More than 50 measurements were carried out at different locations to minimize the microstructural and grain boundary effects.

Fabrication of HEB composite coating and membrane

The prepared HEB composite powders [40 weight % (wt %)], toluene (45 wt %), and fish oil (0.5 wt %) were weighed and milled for 3 hours. After the milling, benzyl butyl phthalate (8.5 wt %) and polyvinyl butyral (6 wt %) were added and milled for 6 hours to form a slurry. The slurry was coated on the drill bit or cast onto a

polyethylene terephthalate sheet, and squares (10 mm) were cut and preheat-treated at 300°C for 1 hour. The coating was densified at 3000 K with multiple-pulse ultrahigh-temperature sintering. The free-standing membrane was sintered at 3000 K, and the duration was adjusted to 5 s.

SUPPLEMENTARY MATERIALS

Supplementary material for this article is available at https://science.org/doi/10.1126/sciadv.abn8241

REFERENCES AND NOTES

1. J. Gild, Y. Zhang, T. Harrington, S. Jiang, T. Hu, M. C. Quinn, W. M. Mellor, N. Zhou, K. Vecchio, J. Luo, High-entropy metal diborides: A new class of high-entropy materials and a new type of ultrahigh temperature ceramics. *Sci. Rep.* **6**, 2–11 (2016).
2. M. Qin, J. Gild, H. Wang, T. Harrington, K. S. Vecchio, J. Luo, Dissolving and stabilizing soft WB2 and MoB2 phases into high-entropy borides via boron-metals reactive sintering to attain higher hardness. *J. Eur. Ceram. Soc.* **40**, 4348–4353 (2020).
3. J. Gild, K. Kaufmann, K. Vecchio, J. Luo, Reactive flash spark plasma sintering of high-entropy ultrahigh temperature ceramics. *Scr. Mater.* **170**, 106–110 (2019).
4. V. Braic, A. Vladescu, M. Balaceanu, C. R. Luculescu, M. Braic, Nanostructured multi-element (TiZrNbHfTa)N and (TiZrNbHfTa)C hard coatings. *Surf. Coatings Technol.* **211**, 117–121 (2012).
5. L. Feng, W. G. Fahrenholtz, G. E. Hilmas, Y. Zhou, Synthesis of single-phase high-entropy carbide powders. *Scr. Mater.* **162**, 90–93 (2019).
6. J. Zhou, J. Zhang, F. Zhang, B. Niu, L. Lei, W. Wang, High-entropy carbide: A novel class of multicomponent ceramics. *Ceram. Int.* **44**, 22014–22018 (2018).
7. T. Jin, X. Sang, R. R. Unocic, R. T. Kinch, X. Liu, J. Hu, H. Liu, S. Dai, Mechanochemical-assisted synthesis of high-entropy metal nitride via a soft urea strategy. *Adv. Mater.* **30**, 1–5 (2018).
8. C. Oses, C. Toher, S. Curtarolo, High-entropy ceramics. *Nat. Rev. Mater.* **5**, 295–309 (2020).
9. A. P. Tomsia, M. Rühle, D. R. Clarke, Annual review of materials research: Introduction. *Annu. Rev. Mat. Res.* **38**, (2008).
10. K. Hofmann, R. Gruehn, B. Albert, Probing for structural features of boron-rich solids with EELS. *Zeitschrift fur Anorg. und Allg. Chemie* **628**, 2691–2696 (2002).
11. G. Tallarita, R. Licheri, S. Garroni, R. Orrù, G. Cao, Novel processing route for the fabrication of bulk high-entropy metal diborides. *Scr. Mater.* **158**, 100–104 (2019).
12. P. H. Mayrhofer, A. Kirnbauer, P. Ertelthaler, C. M. Koller, High-entropy ceramic thin films, a case study on transition metal diborides. *Scr. Mater.* **149**, 93–97 (2018).
13. J. Gild, A. Wright, K. Quiambao-Tomko, M. Qin, J. A. Tomko, M. S. bin Hoque, J. L. Braun, B. Bloomfield, D. Martinez, T. Harrington, K. Vecchio, P. E. Hopkins, J. Luo, Thermal conductivity and hardness of three single-phase high-entropy metal diborides fabricated by borocarbothermal reduction and spark plasma sintering. *Ceram. Int.* **46**, 6906–6913 (2020).
14. Y. Zhang, S. K. Sun, W. Zhang, Y. You, W. M. Guo, Z. W. Chen, J. H. Yuan, H. T. Lin, Improved densification and hardness of high-entropy diboride ceramics from fine powders synthesized via borothermal reduction process. *Ceram. Int.* **46**, 14299–14303 (2020).
15. A. K. Khanra, M. M. Godkhindi, L. C. Pathak, Comparative studies on sintering behavior of self-propagating high-temperature synthesized ultra-fine titanium diboride powder. *J. Am. Ceram. Soc.* **88**, 1619–1621 (2005).
16. S. H. Kang, D. J. Kim, E. S. Kang, S. S. Baek, Pressureless sintering and properties of titanium diboride ceramics containing chromium and iron. *J. Am. Ceram. Soc.* **84**, 893–895 (2001).
17. M. A. Einarsrud, E. Hagen, G. Pettersen, T. Grande, Pressureless sintering of titanium diboride with nickel, nickel boride, and iron additives. *J. Am. Ceram. Soc.* **80**, 3013–3020 (1997).
18. H. Schmidt, G. Borchardt, S. Weber, H. Scherrer, Diffusion in transition metal diborides - an overview. *Defect Diffus. Forum.* **263**, 219–224 (2007).
19. L. Feng, W. G. Fahrenholtz, G. E. Hilmas, Processing of dense high-entropy boride ceramics. *J. Eur. Ceram. Soc.* **40**, 3815–3823 (2020).
20. S. C. Zhang, G. E. Hilmas, W. G. Fahrenholtz, Pressureless densification of zirconium diboride with boron carbide additions. *J. Am. Ceram. Soc.* **89**, 1544–1550 (2006).
21. S. Zhu, W. G. Fahrenholtz, G. E. Hilmas, S. C. Zhang, Pressureless sintering of zirconium diboride using boron carbide and carbon additions. *J. Am. Ceram. Soc.* **90**, 3660–3663 (2007).
22. W. G. Fahrenholtz, G. E. Hilmas, S. C. Zhang, S. Zhu, Pressureless sintering of zirconium diboride: Particle size and additive effects. *J. Am. Ceram. Soc.* **91**, 1398–1404 (2008).
23. G. J. Zhang, M. Ando, J. F. Yang, T. Ohji, S. Kanzaki, Boron carbide and nitride as reactants for in situ synthesis of boride-containing ceramic composites. *J. Eur. Ceram. Soc.* **24**, 171–178 (2004).
24. S. C. Zhang, G. E. Hilmas, W. G. Fahrenholtz, Mechanical properties of sintered ZrB_2-SiC ceramics. *J. Eur. Ceram. Soc.* **31**, 893–901 (2011).
25. E. W. Neuman, G. E. Hilmas, W. G. Fahrenholtz, Processing, microstructure, and mechanical properties of zirconium diboride-boron carbide ceramics. *Ceram. Int.* **43**, 6942–6948 (2017).
26. B. Lönnberg, Thermal expansion studies on the group IV-VII transition metal diborides. *J. Less-Common Met.* **141**, 145–156 (1988).
27. K. Cherednichenko, V. Solozhenko, K. Cherednichenko, V. Solozhenko, Thermal expansion of α -boron and some boron-rich pnictides. *Solid State Commun.* **303–304**, 113735 (2019).
28. S. V. Konovalikhin, D. Y. Kovalev, V. I. Ponomarev, Determination of the thermal expansion coefficient of boron carbide $B_{13}C_2$. *High Temp.* **56**, 668–672 (2018).
29. A. T. Lech, C. L. Turner, R. Mohammadi, S. H. Tolbert, R. B. Kaner, Structure of superhard tungsten tetraboride: A missing link between MB_2 and MB_{12} higher borides. *Proc. Natl. Acad. Sci. U.S.A.* **112**, 3223–3228 (2015).
30. A. T. Lech, C. L. Turner, J. Lei, R. Mohammadi, S. H. Tolbert, R. B. Kaner, Superhard rhenium/tungsten diboride solid solutions. *J. Am. Chem. Soc.* **138**, 14398–14408 (2016).
31. G. Akopov, I. Roh, Z. C. Sobell, M. T. Yeung, L. Pangilinan, C. L. Turner, R. B. Kaner, Effects of variable boron concentration on the properties of superhard tungsten tetraboride. *J. Am. Chem. Soc.* **139**, 17120–17127 (2017).
32. H. Wang, C. A. Wang, X. Yao, D. Fang, Processing and mechanical properties of zirconium diboride-based ceramics prepared by spark plasma sintering. *J. Am. Ceram. Soc.* **90**, 1992–1997 (2007).
33. P. Sarker, T. Harrington, C. Toher, C. Oses, M. Samiee, J. P. Maria, D. W. Brenner, K. S. Vecchio, S. Curtarolo, High-entropy high-hardness metal carbides discovered by entropy descriptors. *Nat. Commun.* **9**, 1–10 (2018).
34. Q. Tao, D. Zheng, X. Zhao, Y. Chen, Q. Li, Q. Li, C. Wang, T. Cui, Y. Ma, X. Wang, P. Zhu, Exploring hardness and the distorted sp^2 hybridization of B-B bonds in WB_3. *Chem. Mater.* **26**, 5297–5302 (2014).
35. R. W. Cahn, Phase diagrams for binary alloys: A desk handbook. *Intermetallics* **9**, 539 (2001).
36. V. Domnich, S. Reynaud, R. A. Haber, M. Chhowalla, Boron carbide: Structure, properties, and stability under stress. *J. Am. Ceram. Soc.* **94**, 3605–3628 (2011).
37. H. Okamoto, Comment on B-Ta (boron-tantalum). *J. Phase Equilibria* **14**, 393–394 (1993).
38. H. Okamoto, B-Zr (Boron-Zirconium). *J. Phase Equilibria* **14**, 261–262 (1993).
39. S. S. Ordan'yan, A. I. Dmitriev, K. T. Bizhev, E. K. Stepanenko, Methods of examination and properties of powder material interaction in B4C-Me(V)B2 systems. *Sov. Powder Met. Met. Ceram.* **298**, 834–836 (1987).
40. A. Kirfel, A. Gupta, G. Will, The nature of the chemical bonding in boron carbide, $B_{13}C_2$. I. Structure refinement. *Acta Crystallogr. Sect. B Struct. Crystallogr. Cryst. Chem.* **35**, 1052–1059 (1979).
41. E. Rudy, S. Windisch, Ternary phase equilibria in transition metal-boron-carbon-silicon systems. Part II. Ternary systems. Vol XIII. Phase diagrams of the systems Ti-B-C, Zr-B-C, and Hf-B-C, *AFML Tech. Report, Part 2, Vol. XIII* (1966).
42. B. Lönnberg, T. Lundström, A study of the thermal expansion of samples within the homogeneity ranges of NbB_2 and TaB_2. *J. Less Common Met.* **139**, L7–L10 (1988).
43. Y. B. Paderno, V. V. Odintsov, I. I. Timofeeva, L. A. Klochkov, Thermal expansion of metal dodecaborides. *TVT* **9**, 200–202 (1971).
44. T. Ma, H. Li, X. Zheng, S. Wang, X. Wang, H. Zhao, S. Han, J. Liu, R. Zhang, P. Zhu, Y. Long, J. Cheng, Y. Ma, Y. Zhao, C. Jin, X. Yu, Ultrastrong boron frameworks in ZrB12: A highway for electron conducting. *Adv. Mater.* **29**, 1–7 (2017).
45. B. Albert, H. Hillebrecht, Boron: Elementary challenge for experimenters and theoreticians. *Angew. Chemie - Int. Ed.* **48**, 8640–8668 (2009).
46. L. A. J. Garvie, W. T. Petuskey, P. F. Mcmillan, P. R. Buseck, High-temperature syntheses in the B – C – N – O system. *J. Solid State Chem.* **371**, 365–371 (1997).
47. B. Morosin, T. L. Aselage, R. S. Feigelson, Crystal structure refinements of rhombohedral symmetry materials containing boron-rich icosahedra. *MRS Proc.* **97**, 145 (1987).
48. B. Post, F. W. Glaser, Crystal structure of ZrB12. *JOM* **4**, 631–632 (1952).
49. H. Xie, M. Hong, E. M. Hitz, X. Wang, M. Cui, D. J. Kline, M. R. Zachariah, L. Hu, High-temperature pulse method for nanoparticle redispersion. *J. Am. Chem. Soc.* **142**, 17364–17371 (2020).
50. ASTM C1327, Standard test method for Vickers indentation hardness of advanced ceramics (ASTM Int., 2009); 10.1520/C1327-15R19.2.

Acknowledgments: We acknowledge the support of the Maryland Nanocenter, its Surface Analysis Center, and AIMLab. **Funding:** J.L. at UCSD acknowledges the support of the Air Force Office of Scientific Research (AFOSR) under grant no. FA9550-19-1-0327 in the Aerospace Materials for Extreme Environments program and program manager, A. Sayir. **Author contributions:** L.H. and H.X. designed the experiments. H.X., M.H., and M.G. carried out the synthesis. H.X. carried out the morphology characterization and composition analysis. H.X. and J.R. worked on the TEM diffraction analysis. M.Q. and J.L. carried out the hardness test. L.H. and H.X. collectively wrote the paper. J.L. revised the paper. All authors commented on the final manuscript. **Competing interests:** The authors declare that they have no competing interests. **Data and materials availability statement:** All data needed to evaluate the conclusions in the paper are present in the paper and/or the Supplementary Materials.

Submitted 23 December 2021
Accepted 23 May 2022
Published 6 July 2022
10.1126/sciadv.abn8241